Nano Research

Open Access

Research Article

High selectivity of H_2O_2 activation to $\cdot O_2^-$ for efficient NO oxidation over Co single-atom catalyst

Zhengyang Gao, Zheng Song, Ziwei Miao, Chenliang Ye ✉, and Weijie Yang ✉

School of Energy and Power Engineering, North China Electric Power University, Baoding 071003, China

Cite this article: *Nano Research*, **2025**, *18*, 94907255. https://doi.org/10.26599/NR.2025.94907255

ABSTRACT: NO oxidation with H_2O_2 as the oxidant is a promising green denitration technology. However, the current metal oxide catalysts still have many disadvantages for this reaction, such as insufficient catalytic activity for H_2O_2 activation, poor selectivity, and low stability. In this study, we employ atomically dispersed Co anchored on SBA-15 with Co-O_4 structure for NO oxidation, which achieves a 90% removal efficiency of NO under low molar ratio of H_2O_2 to NO (1.56), ultra-low temperature (80 °C), and ultra-high space velocity (720,000 h^{-1}), representing the top-level performance among previously reported catalysts. More interestingly, our work reveals that by taking advantage of the uniform Co-O_4 structure, H_2O_2 is mainly directionally converted into $\cdot O_2^-$ at the Co-O_4 site, and $\cdot O_2^-$ plays a key role for achieving the deep-oxidation of NO to produce NO_3^-, which is contrast to the previously reports that $^1O_2$ is the main free radical for NO oxidation. This study highlights the great potentials of single-atom catalysts for improving the H_2O_2 utilization performance for NO oxidation.

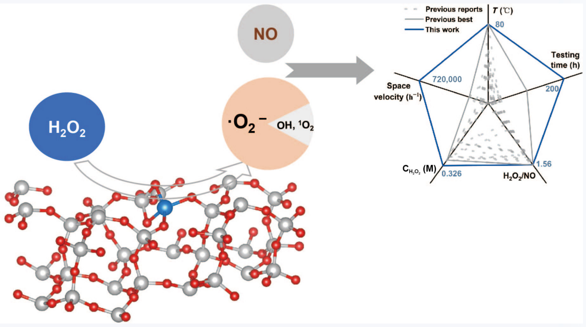

KEYWORDS: Co single-atom catalyst, NO oxidation, H_2O_2 activation, free radical

1 Introduction

NO_x (95% of NO) is one of the main pollutants in the atmosphere, giving rise to haze, acid rain, photochemical pollution and ozone layer depletion, and is extremely detrimental to environment and human health [1–3]. Currently, the selective catalytic reduction (SCR) technology is the most widely used method for reducing NO_x [4]. Nevertheless, this approach requires a high operating temperature window (300–400 °C) and cannot meet emission requirements under complex variable operating conditions. The spent catalyst is biotoxic due to the presence of V, Cr, Ni, and As [5]. Moreover, clogging of downstream flue equipment clogging caused by ammonia escape increases equipment maintenance costs [6]. Therefore, it is crucial to develop a low-temperature economical and eco-friendly de-emission method to couple with or even replace the SCR technology. In this regard, advanced oxidation technology (AOP) holds great application prospects.

The oxidation–absorption method is a feasible method for NO removal, which utilizes strong oxidants (NaClO [7], $NaClO_2$ [8], NaS_2O_8 [2], O_3 [9], and H_2O_2) and their derived reactive free radicals (·ClO, $\cdot O_2^-$, SO_4^-, and ·OH) to oxidize NO to readily soluble components (NO_2, HNO_2, and HNO_3) [10]. An alkaline solution is then used to absorb the oxidized NO_x to achieve complete removal. Hydrogen peroxide, being a cost-effective and environmentally friendly chemical oxidizer, yields nothing but water as the by-product after the oxidation process. Currently, ultraviolet (UV) light [11], ultrasound [12], and transition metals are cross-used to activate H_2O_2. Due to the high energy consumption and the lack of easy amplification of UV light and ultrasound, the use of catalyst heterogeneous activation offers the best industrial prospects. In general, investigations on the simultaneous removal of NO_x with H_2O_2/heterogeneous catalyst are limited. When most catalysts achieve NO removal efficiencies of about 90%, the utilization of H_2O_2 (molar ratio of H_2O_2/NO), the ability of the catalysts to handle flue gases (space velocity), and the lifetime become the key elements limiting the application. Liu et al. investigated the simultaneous removal of NO_x and SO_2 in $NH_3\cdot H_2O$ solution with $Fe_2(MoO_4)_3$ catalyst, and the optimum nitrogen removal rate reached 91.4%, and H_2O_2/NO achieved the lowest value of 1.5 at present. However, the airspeed was low, and the rate of nitrogen removal was slightly decreased in the 15 h test [13]. In addition, it is necessary to further explore a more efficient catalyst for

---

Received: December 9, 2024; **Revised:** January 11, 2025
Accepted: January 13, 2025

✉Address correspondence to Weijie Yang, yangwj@ncepu.edu.cn; Chenliang Ye, chenliangye@ncepu.edu.cn

simultaneous NO_x removal that is stable in long-term operation [14].

Previously, it was understood that ·OH induced NO oxidation is the most efficient reaction pathway in Fenton or Fenton-like AOP systems [13]. Regarding the reactivity of various reactive oxygen species (ROS), an increasing number of researchers have realized that non-radical single-linear oxygen species ($^1O_2$) have longer lifetimes (4 μs), higher selectivity, and stronger reactivity. It exhibits superior capabilities (shorter lifetimes, 10–3 μs, and non-selective) to ·OH in the degradation of organic pollutants in water. Thus, $^1O_2$ has drawn increasing attention [15, 16]. In terms of NO oxidation, Hao et al. proposed the effective role of $^1O_2$ in the oxidation of NO using catalyst-catalyzed H_2O_2 [17]. However, compared with $^1O_2$ (E_0 = 1.52 V) [18, 19], $·O_2^-$ (E_0 = 2.4 V) not only has a higher redox potential but also can generate $^1O_2$ [20]. Most catalysts yield a diverse range of activation products from H_2O_2, and choosing a free radical that can effectively oxidize NO for highly selective directional activation is the optimal approach to address the current issues of low catalyst activity and low utilization efficiency of H_2O_2.

Due to the complex and numerous active sites of metal clusters and nanoparticles (NPs), the activation pathways of H_2O_2 are not uniform, which leads to differences in the types of live ROS produced. However, the current challenge is to understand the mechanism of action of ROS, focusing on the types of ROS that play a key role in pollutant degradation. In this context, Hu et al. embedded single-atom Co into a BCN matrix to achieve 100% conversion of peroxymonosulfate to single-linear oxygen [21]. Through various advanced characterization measurements, metal single-atom catalysts (SACs) can provide more accurate and homogeneous ligand structures of catalytic sites than metal NPs, which is crucial for highly selective directional production of pollutant-targeted ROS, the action mechanisms of different free radicals on NO, and the design principles of catalysts in the future [22–25].

Here, with SBA-15 as the catalyst supports, we prepare Co single-atom catalysts (CoSACs) on a large scale through simple milling and calcination. By means of precise characterization of CoSACs, the uniform Co-O_4 sites on its surface are identified. The CoSACs exhibit excellent catalytic performance for NO oxidation with H_2O_2 as the oxidant, which achieves a 90% removal efficiency of NO under low molar ratio of H_2O_2 to NO (1.56), ultra-low temperature (80 °C), and ultra-high space velocity (720,000 h^{-1}). Moreover, experimental and theoretical calculation results indicate that H_2O_2 is mainly directionally converted into $·O_2^-$ at the Co-O_4 site, and $·O_2^-$ plays a key role for achieving the deep-oxidation of NO to produce NO_3^-, which is contrast to the previously reports that $^1O_2$ is the main free radical for NO oxidation. Among the three kinds of free radicals, $^1O_2$ exhibits the highest reactivity with NO, and the resulting product is NO_2, which is another pollutant gas. $·O_2^-$ is capable of directly and thoroughly oxidizing NO to stable substances. This process effectively averts the secondary pollution induced by intermediate unstable products and elevates the removal efficiency of NO. Furthermore, $^1O_2$ that subsequently generated by a portion of $·O_2^-$ also contributes significantly to the removal of NO.

2 Experimental

Materials: All chemicals were used as received without further purification. Tetraethylorthosilicate (TEOS) and $Co(NO_3)_2·6H_2O$ were purchased from Sinopharm Chemical Reagent Co., Ltd. Pluronic P123 ($EO_{20}PO_{70}EO_{20}$, M_n = ~ 5800) and hydrochloric acid (HCl, 37%) were procured from Sigma-Aldrich Co., Ltd. Deionized water was used throughout this study.

Synthesis of the SBA-15: In a typical procedure, Pluronic P123 (2.0 g) was dissolved into the aqueous HCl solution (1.60 M, 75.0 g). TEOS (4.25 g) was added and stirred at 40 °C for 24 h, followed by the hydrothermal treatment at 100 °C for 24 h. After filtration and then drying under ambient conditions, the template-occupied SBA-15 was recovered. SBA-15 was obtained by calcining at 550 °C for 3 h under an air flow rate of 200 mL·min^{-1} to remove the template agent.

Synthesis of CoSACs and CoNPs: The template-occupied SBA-15 (5 g) and $Co(NO_3)_2·6H_2O$ (0.175 g) were added to a ball mill jar and milled at 500 r·min^{-1} for 20 min to obtain the sample. The catalyst CoSACs were obtained after calcination at 550 °C under air flow (200 mL·min^{-1}) for 3 h to remove the templating agent. For comparison, $Co(NO_3)_2·6H_2O$ (2 g) was used to obtain CoNPs as described above. By introducing a larger ball mill, large-scale preparation can be achieved.

General experimental procedure: It consisted of three parts in Fig. S1 in the Electronic Supplementary Material (ESM): the simulated flue gas generation unit, the catalytic oxidation-absorption unit, and the exhaust gas detection unit. The simulated flue gas consisted of N_2, NO, CO_2, and O_2 with the total flow rate of 2 L·min^{-1}, controlled by reducing valves and mass flow controllers. H_2O_2 solution was injected into Vaporizing tube (quartz spiral tube, inner diameter 2 mm) using an injection pump to generate H_2O_2 vapor. The vapor mixed with the flue gas and enters the catalytic oxidation reactor. NO is oxidized in a U-shaped glass tube (with an inner diameter of 1 cm and a length of 30 cm) heated by an oil bath. The removal of NO after the oxidation products was absorbed by $(NH_4)_2SO_3$ (0.5 M, 500 mL) or deionized water (100 mL) was shown as removal efficiency and oxidation efficiency, respectively. The default working condition was that the hydrogen peroxide concentration was 0.326 mol·L^{-1}, the injection rate was 200 μL·min^{-1}, the vaporization temperature was controlled by an oil bath at 140 °C, the catalytic temperature was 80 °C, the balance gas was N_2, and the total gas flow rate was 2 L·min^{-1}. According to specific experiments, the corresponding conditions were changed. Under default conditions, the saturated water vapor pressure in the system corresponded to a temperature of 51 °C. 0.1 g of catalyst was used for each experiment and fixed with quartz wool. The concentration of NO was 500 ppm. The mesh size of the catalyst was between 40–60 mesh to prevent clogging of the tubes, while the gas hourly space velocity (GHSV) was 720,000 h^{-1}. The flue gas concentration was recorded by a Portable Gas Analyzer (RW5), and the NO removal efficiency was calculated via Eq. (1), and the molar ratio of H_2O_2/NO was obtained via Eq. (2)

$$\text{Removal or oxidation efficiency} = \frac{C_{\text{in}} - C_{\text{out}}}{C_{\text{in}}} \times 100\% \tag{1}$$

$$\text{Molar ratio of } H_2O_2 \text{ to NO} = \frac{22.4\,(273 + T)\, C_{H_2O_2} V_{H_2O_2}}{1000 \times 273 C_{NO} G} \tag{2}$$

where C_{in} and C_{out} are the inlet and outlet concentrations (ppm) of NO, respectively; T, $C_{H_2O_2}$, $V_{H_2O_2}$, C_{NO}, and G are the ambient temperature (°C), H_2O_2 concentration (mol·L^{-1}), H_2O_2 adding rate (mL·min^{-1}), inlet NO concentration (ppm), and total gas flow rate (L·min^{-1}), respectively.

Characterizations: The morphology of the materials was identified by transmission electron microscopy (TEM) (JEM-F200, Japan) and aberration-corrected scaning TEM (STEM) (Thermo Scientific spectra 300, USA). X-ray diffraction (XRD) was recorded on a Bruker D8 Avance diffractometer operated at 40 kV and 40 mA using a Cu Kα radiation (λ = 0.15406 nm) at a step width of 1 °·min^{-1} . X-ray photoelectron spectroscopy (XPS) of all samples was conducted using a Thermo Scientific ESCALAB 250Xi instrument. XPS (ESCALAB 250, Thermo Fisher Scientific, USA) was employed to analyze the surface elements of the samples. The Co K-edge X-ray adsorption fine structure spectroscopy (XAFS) were collected at the 1W1B beamline of Beijing Synchrotron Radiation Facility (BSRF, Beijing, China) using a transmission mode. Electronic paramagnetic resonance (EPR) analysis was performed on a Bruker EMX Plus spectrometer. In the EPR experiment, the conditions were consistent with those of the denitration experiment. 1% H_2O_2 was used, and the temperature was set at 80 °C. In the EPR spectra of $^1O_2$ in the presence of BQ, the addition amount of p-benzoquinone followed the standard of the quenching experiment, which was 90 mM. The Brunauer–Emmett–Teller (BET) surface area was measured by an Autosorb-I-MP system. The BET surface area was measured by an American Mack ASAP 2460 analyzer. The actual compositions of sample were determined by inductively coupled plasma-optical emission spectroscopy (ICP-OES) technique (PE-7000, USA).

Theoretical calculations: All density functional theory (DFT) calculations were carried out with the Vienna *ab initio* Simulation Package (VASP). All calculations used the projector augmented wave (PAW) method [26]. Exchange correlation interactions were handled using the generalized gradient approximation (GGA) [27] method and the Perdew-Burke Ernzerhof (PBE) [27] functional. Based on the DFT-D3 framework [28], van der Waals interactions corrections were taken into consideration. For the SACs model, the catalyst surface was simulated using 5 × 3√3 × 1 graphene with a vacuum layer of 20 Å [29]. Geometric optimizations were conducted using a 450 eV energy cutoff and a 2 × 2 × 1 Γ-centered *k*-point. For each atom, the force criteria requirements were set at 0.02 eV·Å^{-1}. To get accurate information on the electronic configuration as well as energy in the ground state, a 4 × 4 × 1 *k*-point grid was used with a convergence threshold of 10^{-5} eV for electronic self-consistent calculations [30]. The Bader charge analysis method was utilized for the charge analysis. We use the following formula to calculate the desorption energy (E_{des}) (Eq. (3))

$$E_{\text{des}} = E_{\text{sur}} + E_{\text{gas}} - E_{\text{absorb}} \tag{3}$$

E_{sur} represents surface energy; E_{gas} represents gas energy, and E_{adsorb} represents adsorption energy.

Through research and calculation, we obtained the adsorption intensities of five free radicals. Among them, O_2, $^1O_2$, and $\cdot O_2^-$ were distinguished in a series of calculations. O_2 and $^1O_2$ were distinguished by changing the bond length. The initial bond length of O_2 is set to 1.2075 (experimental data from National Institute of Standards and Technology (NIST)), and MAGMOM = 2*2. The initial bond length of $^1O_2$ is set to 1.26, and NUODOWN = 0. For $\cdot O_2^-$, we used the method of neutralizing electrons for calculation. The detailed calculation information was shown in Tables S5–S8 in the ESM.

3 Results and discussion

3.1 Catalysts characterizations

A concentrated peak along with two weak ones, corresponding to (100), (110), and (200) reflections, respectively, can be identified in the low-angle XRD patterns of all samples (Fig. 1(a)). This reflects that two-dimensional hexagonal pore symmetry is well kept after

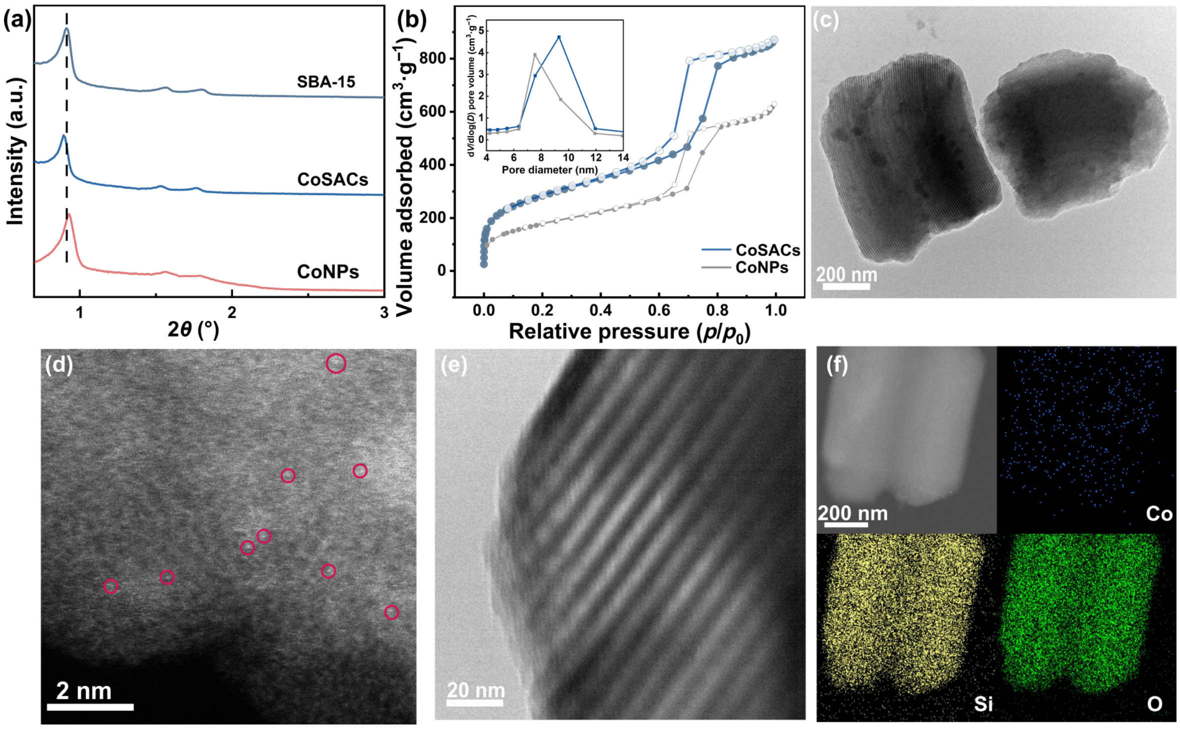

Figure 1 (a) Low-angle XRD patterns of SBA-15, CoSACs, and CoNPs. (b) N_2 adsorption desorption isotherms of CoSACs and CoNPs. Inset: pore size distributions of CoSACs and CoNPs. (c) High-magnification TEM image of CoNPs. (d) Spherical aberration corrected HAAFD-STEM image of CoSACs. Typical Co single atoms are marked by red circles. (e) High-magnification TEM image of CoSACs. (f) EDS element mapping images of CoSACs.

the loading of Co. Comparing with CoSACs, the CoNPs samples show weaker peak of (110) and (200) reflections, which indicates the introduction of a large amount of Co occupies part of the channel space and reduces the pore symmetry degree of mesoporous structure [31]. All the samples displayed type IV isotherms with well-defined H1-type hysteresis loops in N_2 sorption isotherms (Fig. 1(b)), which reflects an ordered mesostructure with cylindrical mesopores [32]. A broad diffraction peak between 15° and 23° appeared for all the samples in XRD patterns (Fig. S2 in the ESM), which was ascribed to the amorphous silica. No diffraction peaks of metallic Co or Co oxide are observed for the obtained catalysts, even for CoNPs, indicating that Co species are dispersed well within SBA-15 mesopores [33, 34].

TEM images show the periodic mesoporous structure with black and white stripes in CoSACs and CoNPs (Figs. 1(c) and 1(e), and Figs. S3 and S4 in the ESM). No CoO_x nanoparticles were observed in CoSACs. Energy-dispersive X-ray spectroscopy (EDS) mappings reveal the uniform distribution of Co composition in SBA-15. The microstructure of CoSACs is further characterized by spherical aberration-corrected high-angle annular dark-field-scanning transmission electron microscopy (HAADF-STEM). It can be seen that the Co species are dominantly present in the form of single atoms rather than clusters or nanoparticles (Fig. 1(d)). In comparison, there were some places with larger dark contrast and small dark spots in CoNPs due to the aggregation of metal oxide particles (Fig. S4 in the ESM) [32]. The loadings of Co in CoSACs and CoNPs were 1.04 wt.% and 9.97 wt.%, respectively, according to ICP-OES results (Table S1 in the ESM). Due to the large introduction of Co in CoNPs, Co peaks appeared in XPS survey spectrum (Fig. S5 in the ESM). CoNPs exhibited a smaller average pore volume (0.956 $cm^3 \cdot g^{-1}$) than CoSACs (1.24 $cm^3 \cdot g^{-1}$), which results from the supported Co species that reduce the pore volume (Table S1 in the ESM).

XPS was applied to characterize valence state of CoSACs and CoNPs (Fig. 2(a)). The high-resolution Co 2p spectra exhibited four deconvoluted peaks with binding energies of 781.89 and 797.50 eV assigned to Co^{2+} $2p_{3/2}$ and Co^{2+} $2p_{1/2}$ [35], and binding energies of 783.02 and 799.06 eV assigned to Co^{3+} $2p_{3/2}$ and Co^{3+} $2p_{1/2}$ [36]. Therefore, it can be concluded that CoNPs demonstrate the coexistence of Co^{2+} and Co^{3+} species, and only Co^{2+} species are detected for CoSACs. To identify the precise structure of the samples, extended XAFS (EXAFS) was conducted to investigate the local coordination environment of Co. The Co K-edge XANES spectra (Fig. 2(c)) show that the absorption edge position of CoSACs located between the Co foil and Co_3O_4, indicating that the valence state of the Co atom was between 0 and +3 [37]. The Fourier-transformed (FT) k^2-weighted EXAFS spectra (Fig. 2(b)) display one main peak at 1.5 Å, corresponding to the Co–O first coordination shell, and no Co–Co coordination peak at 2.2 Å can be detected [38], suggesting the Co species are well isolated. These results are also confirmed by the wavelet transforms (WT). As shown in Fig. 2(f), the intensity maximum of CoSACs is far away from that of Co foil and quite different from that of Co_3O_4, excluding the presence of agglomerated Co or CoO_x in the sample. By fitting the EXAFS spectra, the precise coordination environment of Co is obtained (Figs. 2(d) and 2(e) and Table S2 in the ESM) [39]. The Co–O coordination number of CoSACs is 4.1, indicating the formation of Co-O_4 structure.

3.2 Heterogeneous Fenton denitrification performance

The catalytic activity of the catalyst for NO removal under diverse conditions was examined. In the absence of catalysts, the extremely low concentration of H_2O_2 and the molar ratio of H_2O_2/NO result in a maximum nitrogen removal of only 5%, indicating that hydrogen peroxide alone has a weak ability to oxidize NO [40]. However, the presence of the catalyst significantly improved the NO removal efficiency. The experiment shows that SBA-15 has no catalytic effect on H_2O_2, excluding the judgment that the substrate

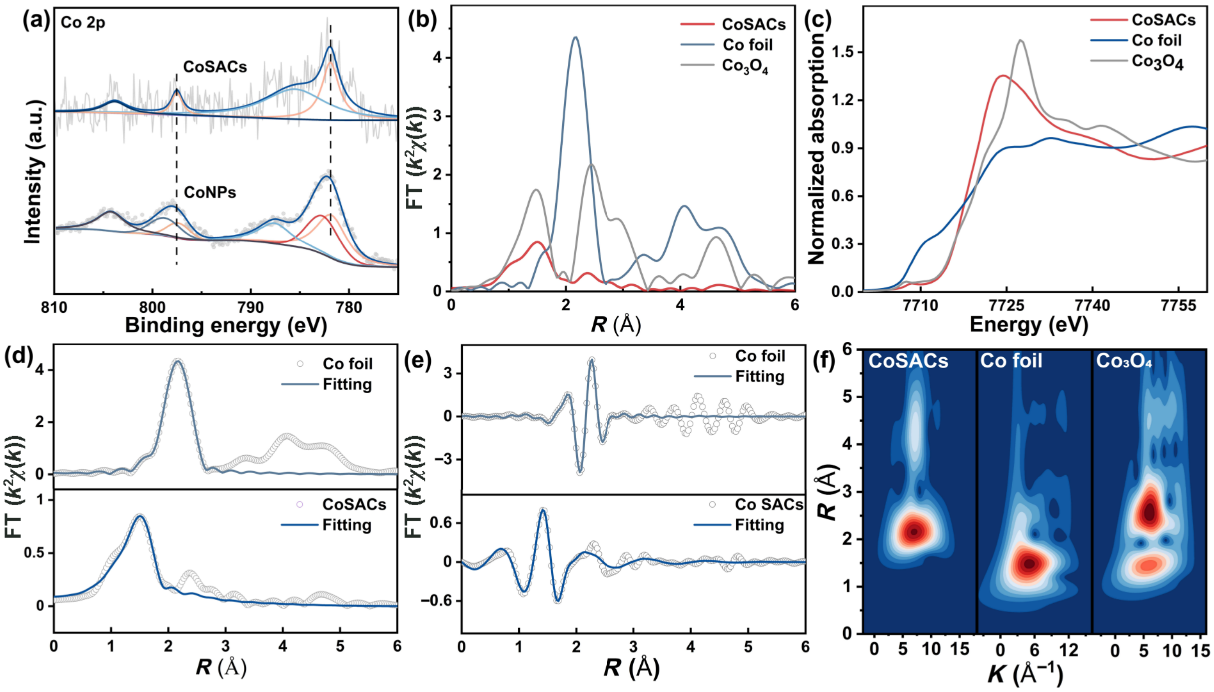

Figure 2 X-ray spectral analysis. (a) Co 2p XPS spectra of CoSACs and CoNPs. (b) and (c) Fourier transform of k^2-weighted EXAFS spectra of CoSACs and CoNPs in reference to Co foil and Co_3O_4 and normalized Co K-edge XANES. (d) and (e) Fourier transform of k^2-weighted EXAFS R space magnitude and imaginary fitting results of Co K-edge for CoSACs and Co foil. (f) Wavelet transforms for the k^2-weighted Co K-edge EXAFS spectra of CoSACs, Co foil and Co_3O_4, respectively.

itself has an active site. The influence of temperature on the catalytic activity was investigated within the range from 60 to 180 °C (Fig. 3(a)). Both samples exhibited better catalytic performance at low temperatures. CoSACs showed the optimal performance at 80 °C, with an oxidation efficiency of 80% and a removal efficiency of 90%. Compared with CoSACs, CoNPs demonstrated a large performance gap under all conditions. This might be due to the non-homogeneous active sites of CoNPs. Besides, XPS results show that CoNPs have mixed valence Co species which will result in fewer highly selective active sites. The more regular mesopore structure and pore size of CoSACs favor the diffusion of NO in the pore channels, and the larger specific surface area facilitates the loading of more Co-O_4 sites. The effect of airspeed on catalytic activity was also examined (Fig. 3(b) and Table S9 in the ESM). To exclude the influence of changes in alkaline absorbent concentration and contact times resulting from gas flow rates, only the oxidation rate of NO is compared [41, 42]. As the airspeed increases (the molar ratio of H_2O_2/NO = 1.56), the residence time of NO on CoSACs becomes shorter and the oxidation efficiency decreases. More NO_2 is produced indicating a decrease in the depth of oxidation [43]. This airspeed range has less impact on the catalytic efficiency of CoNPs, probably due to the high loading of Co to form multiple and heterogeneous active sites, but fewer sites with high selective performance of activated H_2O_2, resulting in a large gap between the performances and CoSACs. The effect of the molar ratio of H_2O_2/NO on the catalyst was investigated by varying the concentration of H_2O_2 (Fig. 3(c)). When the molar ratio of H_2O_2/NO was increased from 0.78 to 1.56, the NO removal increased from 55% to 90%. A molar ratio of 1.56 was selected as the optimum condition. The excellent performance of the catalyst at low concentrations of H_2O_2 can be attributed to the excellent water resistance and high activity. The effect of pH of H_2O_2 was also examined, and at low pH (Fig. 3(e)), good activity was maintained in alkaline environments due to the facilitating effect of more H^+. The effect of O_2 and CO_2 on the efficiency of the catalyst was almost negligible (Fig. 3(d) and Fig. S6 in the ESM). The stability of the catalyst was evaluated. After 200 h of testing, the NO removal efficiency decreased by only 10%. Comparison of XPS fine spectra between fresh catalyst and after 50 h of use showed no significant change, indicating good stability of the catalyst (Fig. S7 in the ESM). Compared with the performance data in previous literature, CoSACs have outstanding performance advantages (Fig. 3(f) and Table S4 in the ESM).

3.3 ROS determination and quenching experiments

EPR test was conducted to determine the species of free radicals generated by H_2O_2 activation (Fig. 4(a)). The fingerprint peaks of 5,5-dimethyl-1-pyrroline-N-oxide-hydroxyl adduct (DMPO-OH) (1:2:2:1), DMPO-$\cdot O_2^-$ (sextet line signals), and 2,2,6,6-tetramethyl-4-piperidinol-N-oxyl (TEMPO, triple line signals) adducts confirm the formations of ·OH, $\cdot O_2^-$, and $^1O_2$. The peak intensities of $^1O_2$ and $\cdot O_2^-$ are higher than those of ·OH, suggesting that $^1O_2$ and $\cdot O_2^-$ are the dominant ROS [44]. The signals of the three ROS were stronger over time at 10 min, suggesting continued production of ROS (Fig. S8 in the ESM). Quenching experiments were conducted to further identify the major ROS (Fig. 4(b)) [17, 44]. Various quenchers, including methanol (MeOH), L-Histidine (His), and p-benzoquinone (p-BQ), were used to capture ·OH, $^1O_2$, and $\cdot O_2^-$, respectively [17, 45]. Unlike the previous recognition of ·OH as the optimal radical for NO removal, MeOH and His significantly inhibited NO oxidation, especially His. The inhibition rates were His (66%) > BQ (38%) > TBA (6%) in descending order, suggesting that the order of contribution of ROS to the NO removal rate was $\cdot O_2^-$ > $^1O_2$ > ·OH. Since the total inhibition rate is greater than the oxidation rate, it needs to be taken into account that $\cdot O_2^-$ is an important precursor for the production of $^1O_2$ [46]. The EPR spectra of TEMP-$^1O_2$ showed no peaks following injection of p-BQ, further verifying that $^1O_2$ is overwhelmingly derived from $\cdot O_2^-$

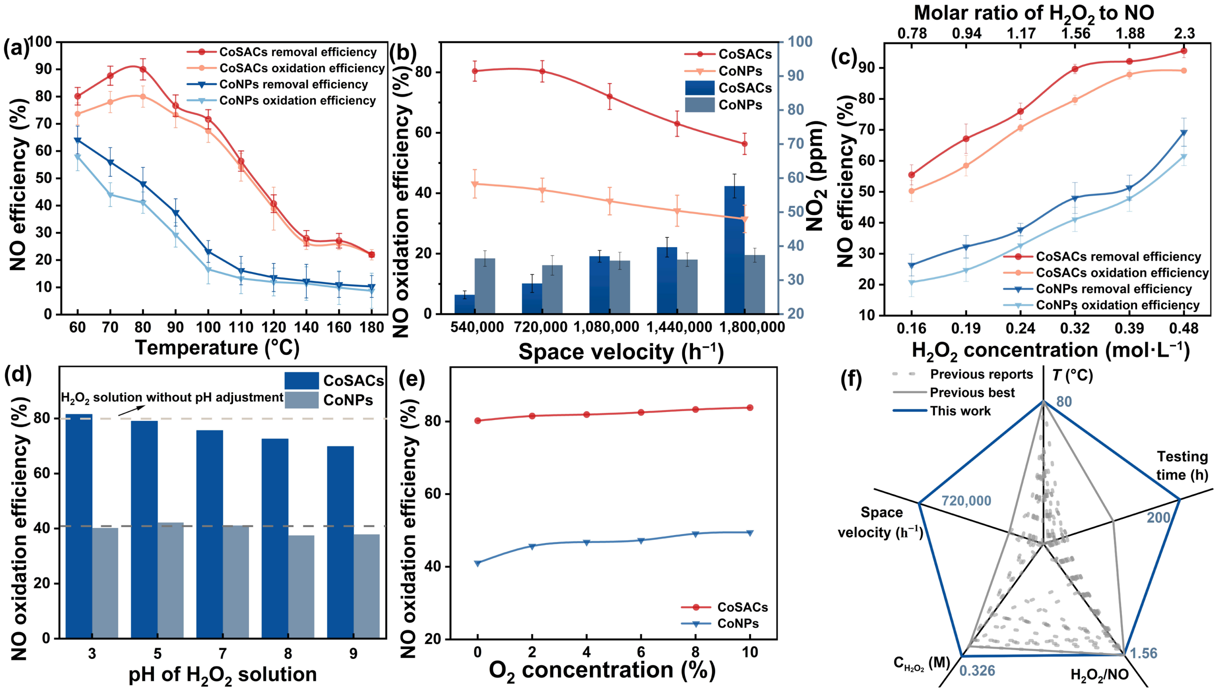

Figure 3 The catalytic performance of different catalysts for NO removal. (a) the influences of temperature. (b) The influence of space velocity on NO removal efficiency. (c) The influence of the molar ratio of H_2O_2/NO, (d) pH of H_2O_2 solution, and (e) the flue gas components (O_2) on the NO removal efficiency. (f) Radar chart of the performance of CoSACs.

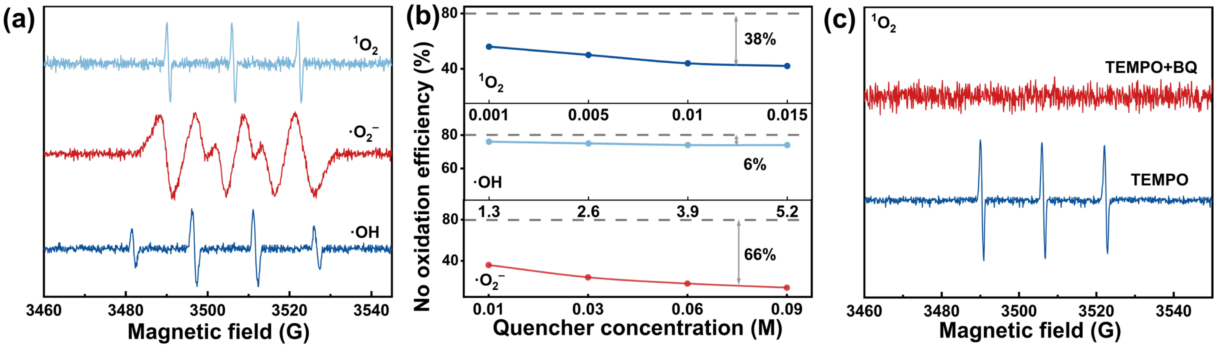

Figure 4 (a) EPR tests with DMPO and TEMP. (b) The radical scavenging experiments. (c) The EPR spectra of $^1O_2$ in the presence of BQ.

instead of H_2O_2 (Fig. 4(c) and Fig. S9 in the ESM). Under the condition of complete $\cdot O_2^-$ quenching, the oxidation efficiency is only 14%. Meanwhile, a blank experiment was conducted without a catalyst, and the oxidation efficiency was only 4%. $\cdot O_2^-$ accounted for 86.84% of all ROS, indicating a highly selective conversion of H_2O_2 to $\cdot O_2^-$.

3.4 Theoretical calculation of the selectivity for H_2O_2 activation

To further identify the dominant product of H_2O_2 activation, the desorption energy of potential free radicals (O_2, $\cdot O_2^-$, $^1O_2$, ·OOH, ·OH) was calculated, as shown in the Fig. 5(a) and Table S3 in the ESM. The desorption energy of free radicals including O_2, $\cdot O_2^-$ and $^1O_2$ is obviously lower than that of ·OH and ·OOH, suggesting that ·OH and ·OOH are unlikely to be the dominant products due to their high desorption energies. The tendency of desorption energy for various free radicals is consistent with the following analysis of charge density differences (Figs. 5(b)–5(d)). Obviously, the isosurface distribution of electron transfer around O_2 is the least noticeable, corresponding to the smallest charge transfer value (0.04 e). Therefore, the lowest desorption energy of $\cdot O_2^-$ over CoSACs can be well understood. In detail, the desorption energy of $\cdot O_2^-$ is 2.35 eV, which is far lower than other free radicals. Due to its lowest desorption energy, $\cdot O_2^-$ is the easiest to desorb among various free radicals, indicating that $\cdot O_2^-$ should be the dominant product of H_2O_2 activation over CoSACs. Importantly, both the theoretical results of desorption energy and the experimental results of radical quenching indicate that $\cdot O_2^-$ is the dominant product of H_2O_2 activation over CoSACs.

Based on the above results of theoretical calculations and experiments, we can confirm that H_2O_2 can be highly selectively and directionally generated to $\cdot O_2^-$ on CoSACs. However, quenching experiments indicate that $^1O_2$ plays a certain role in the oxidation of NO. According to the previous study [20], $\cdot O_2^-$ can be easily converted into $^1O_2$, which can well explain the contribution of $^1O_2$ in the quenching experiments.

Previous studies have shown that ·OH reacting with NO tends to produce HNO_2, while $^1O_2$ reacting with NO tends to produce NO_2. Compared with $^1O_2$ and OH, $\cdot O_2^-$ is capable of carrying out the deepest oxidation with NO, thereby enhancing the removal efficiency of NO. The product is NOs_3^-, reducing the secondary pollution of NO_2. And $^1O_2$ that subsequently generated by a portion of $\cdot O_2^-$ has the easiest reactivity with NO among the three kinds of free radicals [17]. Combined with the experimental results, it shows that directional activation to $\cdot O_2^-$ is a better strategy for removing NO.

4 Conclusions

This study reports the preparation, characterization, and application of Co single-atom catalysts for NO oxidation with H_2O_2 as the oxidant. The uniform and highly active Co-O_4 site of this catalyst promotes the highly selective and directional activation of H_2O_2 to $\cdot O_2^-$. Under specific conditions of a low H_2O_2/NO molar ratio (1.56), high space velocity (720,000 h^{-1}), and ultra-low temperature (80 °C), the CoSACs/H_2O_2 system exhibits economical and effective removal of NO at a conversion of 90%, along with excellent reusability and broad application prospects. Unlike the traditional

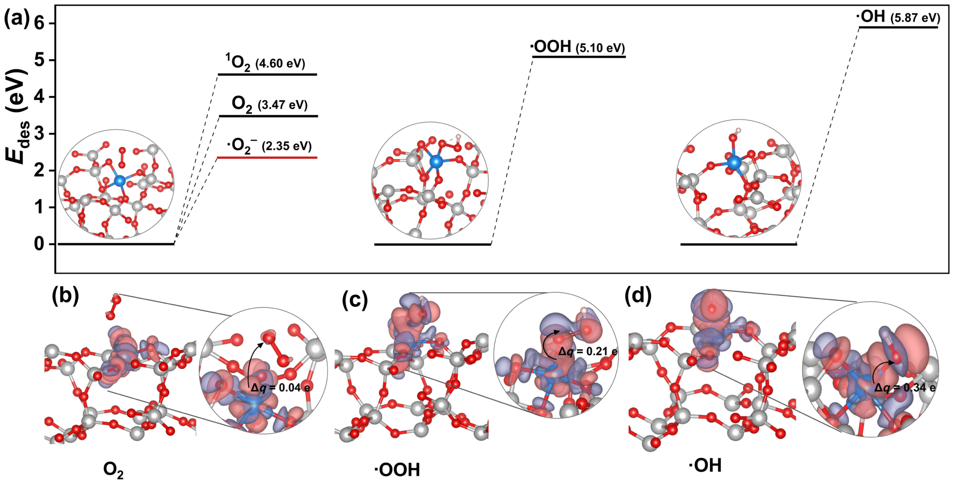

Figure 5 (a) Adsorption intensities of five free radicals. (b)–(d) Charge density differences induced by gas adsorption at the CoSACs (isosurface level: 0.00184612).

Fenton reaction dominated by $^1O_2$, the highly selective and directional generation of $\cdot O_2^-$ has an obvious removal effect on NO. Through a combination of experimental and theoretical calculation methods, the directional generation reason of $\cdot O_2^-$ in the CoSACs/H_2O_2 system and the $\cdot O_2^-$ induced NO removal mechanism are systematically elucidated, which suggests that $\cdot O_2^-$ can complete the deepest oxidation with NO.

Electronic Supplementary Material: Supplementary material (detailed experimental methods, theoretical models, and characterization data) is available in the online version of this article at https://doi.org/10.26599/NR.2025.94907255.

Data availability

All data needed to support the conclusions in the paper are presented in the manuscript and the Electronic Supplementary Material. Additional data related to this paper may be requested from the corresponding author upon request.

Acknowledgements

This work was funded by the National Natural Science Foundation of China (Nos. 52176104 and 52006073), the Natural Science Foundation of Hebei Province (No. B2023502023), and Fundamental Research Fund for the Central Universities (Nos. 2023MS125 and 2024MS154).

Declaration of competing interest

All the contributing authors report no conflict of interests in this work.

Author contribution statement

G. Z. Y.: Conceptualization, methodology, investigation, data curation, visualization, formal analysis, funding acquisition, writing – original draft. Z. S.: Investigation, experimental design, data analysis, writing – original draft. Z. W. M.: Investigation, data curation. C. L. Y.: Supervision, data curation, writing – review & editing. W. J. Y.: Supervision, funding acquisition, project administration, writing – review & editing. All the authors have approved the final manuscript.

Use of AI statement

None.

References

[1] Zhu, S. J.; Lyu, Q. G.; Zhu, J. G.; Wu, H. X.; Wu, G. L. Effect of air distribution on NO_x emissions of pulverized coal and char combustion preheated by a circulating fluidized bed. *Energy Fuels* **2018**, *32*, 7909–7915.

[2] Adewuyi, Y. G.; Sakyi, N. Y. Simultaneous absorption and oxidation of nitric oxide and sulfur dioxide by aqueous solutions of sodium persulfate activated by temperature. *Ind. Eng. Chem. Res.* **2013**, *52*, 11702–11711.

[3] Hailili, R.; Ji, H. W.; Wang, K. W.; Dong, X. A.; Chen, C. C.; Sheng, H.; Bahnemann, D. W.; Zhao, J. C. ZnO with controllable oxygen vacancies for photocatalytic nitrogen oxide removal. *ACS Catal.* **2022**, *12*, 10004–10017.

[4] Wang, B.; Song, Z. J.; Sun, L. S. A review: Comparison of multi-air-pollutant removal by advanced oxidation processes-industrial implementation for catalytic oxidation processes. *Chem. Eng. J.* **2021**, *409*, 128136.

[5] Dai, Z. J.; Wang, L. L.; Tang, H.; Sun, Z. J.; Liu, W.; Sun, Y.; Su, S.; Hu, S.; Wang, Y.; Xu, K. et al. Speciation analysis and leaching behaviors of selected trace elements in spent SCR catalyst. *Chemosphere* **2018**, *207*, 440–448.

[6] Tong, T.; Chen, J. J.; Xiong, S. C.; Yang, W. H.; Yang, Q. L.; Yang, L. J.; Peng, Y.; Liu, Z. M.; Li, J. H. Vanadium-density-dependent thermal decomposition of NH_4HSO_4 on V_2O_5/TiO_2 SCR catalysts. *Catal. Sci. Technol.* **2019**, *9*, 3779–3787.

[7] Mondal, M. K.; Chelluboyana, V. R. New experimental results of combined SO_2 and NO removal from simulated gas stream by NaClO as low-cost absorbent. *Chem. Eng. J.* **2013**, *217*, 48–53.

[8] Park, H. W.; Choi, S.; Park, D. W. Simultaneous treatment of NO and SO_2 with aqueous $NaClO_2$ solution in a wet scrubber combined with a plasma electrostatic precipitator. *J. Hazard. Mater.* **2015**, *285*, 117–126.

[9] Han, C. Y.; Zhang, S. L.; Guo, L. N.; Zeng, Y. Q.; Li, X. H.; Shi, Z. C.; Zhang, Y.; Zhang, B. Q.; Zhong, Q. Ehanced catalytic ozonation of NO over black-TiO_2 catalyst under inadequate ozone (O_3/NO molar ratio = 0.6). *Chem. Eng. Res. Des.* **2018**, *136*, 219–229.

[10] Song, Z. J.; Wang, B.; Yang, W.; Chen, T.; Ma, C.; Sun, L. S. Simultaneous removal of NO and SO_2 through heterogeneous catalytic oxidation-absorption process using magnetic $Fe_{2.5}M_{0.5}O_4$ (M = Fe, Mn, Ti and Cu) catalysts with vaporized H_2O_2. *Chem. Eng. J.* **2020**, *386*, 123883.

[11] Hao, R. L.; Zhao, Y.; Yuan, B.; Zhou, S. H.; Yang, S. Establishment of a novel advanced oxidation process for economical and effective removal of SO_2 and NO. *J. Hazard. Mater.* **2016**, *318*, 224–232.

[12] Liu, Y. X.; Liu, Z. Y.; Wang, Y.; Yin, Y. S.; Pan, J. F.; Zhang, J.; Wang, Q. Simultaneous absorption of SO_2 and NO from flue gas using ultrasound/Fe^{2+}/heat coactivated persulfate system. *J. Hazard. Mater.* **2018**, *342*, 326–334.

[13] Liu, X.; Wang, C. A.; Zhu, T.; Lv, Q.; Li, Y.; Che, D. F. Simultaneous removal of NO_x and SO_2 from coal-fired flue gas based on the catalytic decomposition of H_2O_2 over $Fe_2(MoO_4)_3$. *Chem. Eng. J.* **2019**, *371*, 486–499.

[14] Jia, S. H.; Pu, G.; Gao, J.; Yuan, C. Oxidation-absorption process for simultaneous removal of NO_x and SO_2 over $Fe/Al_2O_3@SiO_2$ using vaporized H_2O_2. *Chemosphere* **2022**, *291*, 133047.

[15] Hong, P. D.; Wu, Z. J.; Yang, D. D.; Zhang, K. S.; He, J. Y.; Li, Y. L.; Xie, C.; Yang, W.; Yang, Y.; Kong, L. T. et al. Efficient generation of singlet oxygen ($^1O_2$) by hollow amorphous Co/C composites for selective degradation of oxytetracycline via Fenton-like process. *Chem. Eng. J.* **2021**, *421*, 129594.

[16] Batchelor, S. N.; Carr, D.; Coleman, C. E.; Fairclough, L.; Jarvis, A. The photofading mechanism of commercial reactive dyes on cotton. *Dyes Pigm.* **2003**, *59*, 269–275.

[17] Qian, Z.; Luo, M. C.; Feng, X. H.; Yang, X. J.; Guo, Y. X.; Yang, L. J.; Yuan, B.; Zhao, Y.; Hao, R. L. Unexpected role of singlet oxygen generated in urea-modulated $LaFeO_3$ perovskite heterogeneous Fenton system in denitrification: Mechanism and theoretical calculations. *Appl. Catal. B: Environ.* **2023**, *338*, 123042.

[18] Guo, R. T.; Hao, J. K.; Pan, W. G.; Yu, Y. L. Liquid phase oxidation and absorption of NO from flue gas: A review. *Sep. Sci. Technol.* **2015**, *50*, 310–321.

[19] Weast, R. C., Ed. *CRC Handbook of Chemistry and Physics*, 57th ed.; CRC Press: Cleveland, OH, USA.

[20] Wang, J. L.; Wang, S. Z. Reactive species in advanced oxidation processes: Formation, identification and reaction mechanism. *Chem. Eng. J.* **2020**, *401*, 126158.

[21] Zhao, X.; Li, X.; Zhu, Z.; Hu, W. B.; Zhang, H. B.; Xu, J.; Hu, X.; Zhou, Y. T.; Xu, M.; Zhang, H. C. et al. Single-atom Co embedded in BCN matrix to achieve 100% conversion of peroxymonosulfate into singlet oxygen. *Appl. Catal. B: Environ.* **2022**, *300*, 120759.

[22] Wang, Y.; Ma, F. Y.; Zhang, G. Q.; Zhang, J. W.; Zhao, H.; Dong, Y. M.; Wang, D. S. Precise synthesis of dual atom sites for electrocatalysis. *Nano Res.* **2024**, *17*, 9397–9427.

[23] Guo, Y. J.; Liu, Z. Y.; Zhou, D. Y.; Zhang, M. Y.; Zhang, Y.; Li, R. Z.; Liu, S. L.; Wang, D. S.; Dai, Z. H. Competition and synergistic effects of Ru-based single-atom and cluster catalysts in electrocatalytic reactions. *Sci. China Mater.* **2024**, *67*, 1706–1720.

[24] Gan, T.; Wang, D. S. Atomically dispersed materials: Ideal catalysts in atomic era. *Nano Res.* **2024**, *17*, 18–38.

[25] Han, A. L.; Sun, W. M.; Wan, X.; Cai, D. D.; Wang, X. J.; Li, F.; Shui, J. L.; Wang, D. S. Construction of Co_4 atomic clusters to enable Fe-N_4 motifs with highly active and durable oxygen reduction performance. *Angew. Chem., Int. Ed.* **2023**, *62*, e202303185.

[26] Perdew, J. P.; Burke, K.; Ernzerhof, M. Generalized gradient approximation made simple. *Phys. Rev. Lett.* **1996**, *77*, 3865–3868.

[27] Kresse, G.; Joubert, D. From ultrasoft pseudopotentials to the projector augmented-wave method. *Phys. Rev. B* **1999**, *59*, 1758–1775.

[28] Grimme, S.; Antony, J.; Ehrlich, S.; Krieg, H. A consistent and accurate *ab initio* parametrization of density functional dispersion correction (DFT-D) for the 94 elements H-Pu. *J. Chem. Phys.* **2010**, *132*, 154104.

[29] Ma, L.; Zhang, J. M.; Xu, K. W.; Ji, V. A first-principles study on gas sensing properties of graphene and Pd-doped graphene. *Appl. Surf. Sci.* **2015**, *343*, 121–127.

[30] Yang, W. J.; Huang, H. Y.; Liu, X. S.; Ren, J. N.; Ma, K.; Pan, Z. H.; Ding, Z.; Ding, X. L.; Gao, Z. Y. Screening the activity of single-atom catalysts for the catalytic oxidation of sulfur dioxide with a kinetic activity model. *Chem. Commun.* **2020**, *56*, 11657–11660.

[31] Baerlocher, C.; McCusker, L. B. Practical aspects of powder diffraction data analysis. *Stud. Surf. Sci. Catal.* **1994**, *85*, 391–428.

[32] Xie, X. W.; Xie, R.; J. Suo, Z. Y.; Huang, H. B.; Xing, M. Y.; Lei, D. X. A highly dispersed Co-Fe bimetallic catalyst to activate peroxymonosulfate for VOC degradation in a wet scrubber. *Environ. Sci.: Nano* **2021**, *8*, 2976–2987.

[33] Feng, X. T.; Shang, Z. A.; Qin, R.; Han, Y. H. Advances in single-atom catalysts for electrocatalytic CO_2 reduction. *Acta Phys. -Chim. Sin.* **2024**, *40*, 2305005.

[34] Wang, M. Y.; Huang, R. B.; Xiong, J. F.; Tian, J. H.; Li, J. F.; Tian, Z. Q. Critical role and recent development of separator in zinc-air batteries. *Acta Phys. -Chim. Sin.* **2024**, *40*, 2307017.

[35] Liang, H. J.; Zhang, B.; Gao, P.; Yu, X. H.; Liu, X. C.; Yang, X. C.; Wu, H. B.; Zhai, L. M.; Zhao, S. C.; Wang, G. F. et al. Strong Co–O–Si bonded ultra-stable single-atom Co/SBA-15 catalyst for selective hydrogenation of CO_2 to CO. *Chem Catal.* **2022**, *2*, 610–621.

[36] Li, X.; Surkus, A. E.; Rabeah, J.; Anwar, M.; Dastigir, S.; Junge, H.; Brückner, A.; Beller, M. Cobalt single-atom catalysts with high stability for selective dehydrogenation of formic acid. *Angew. Chem., Int. Ed.* **2020**, *59*, 15849–15854.

[37] Zhang, R. R.; Sun, Z. T.; Zong, C. C.; Lin, Z. Y.; Huang, H.; Yang, K.; Chen, J.; Liu, S.; Huang, M. X.; Yang, Y. et al. Increase of Co 3D projected electronic density of states in $AgCoO_2$ enabled an efficient electrocatalyst toward oxygen evolution reaction. *Nano Energy* **2019**, *57*, 753–760.

[38] Pan, Y.; Lin, R.; Chen, Y. J.; Liu, S. J.; Zhu, W.; Cao, X.; Chen, W. X.; Wu, K. L.; Cheong, W. C.; Wang, Y. et al. Design of single-atom Co-N_5 catalytic site: A robust electrocatalyst for CO_2 reduction with nearly 100% CO selectivity and remarkable stability. *J. Am. Chem. Soc.* **2018**, *140*, 4218–4221.

[39] Ye, C. L.; Zheng, M.; Li, Z. M.; Fan, Q. K.; Ma, H. Q.; Fu, X. Z.; Wang, D. S.; Wang, J.; Li, Y. D. Electrical pulse induced one-step formation of atomically dispersed Pt on oxide clusters for ultra-low-temperature zinc-air battery. *Angew. Chem., Int. Ed.* **2022**, *61*, e202213366.

[40] Kasper, J. M.; Iii, C. A. C.; Cooper, C. D. Control of nitrogen oxide emissions by hydrogen peroxide-enhanced gas-phase oxidation of nitric oxide. *J. Air Waste Manag. Assoc.* **1996**, *46*, 127–133.

[41] Chen, L.; Yang, W. J.; Wang, Y. G.; Liang, Z. Y.; Zhao, Q. X.; Lu, Q. Investigation on the NO removal from simulated flue gas by using H_2O_2 vapor over $Fe_2(MoO_4)_3$. *Energy Fuels* **2018**, *32*, 8605–8613.

[42] Zhao, Y.; Yuan, B.; Shen, Y.; Hao, R. L.; Yang, S. Simultaneous removal of NO and SO_2 from flue gas using vaporized H_2O_2 catalyzed by nanoscale zero-valent iron. *Environ. Sci. Pollut. Res.* **2018**, *25*, 25526–25537.

[43] Chen, L.; Li, Y. X.; Zhao, Q. X.; Wang, Y. G.; Liang, Z. Y.; Lu, Q. Removal of NO_x using hydrogen peroxide vapor over Fe/TiO_2 catalysts and an absorption technique. *Catalysts* **2017**, *7*, 386.

[44] Nosaka, Y.; Nosaka, A. Y. Generation and detection of reactive oxygen species in photocatalysis. *Chem. Rev.* **2017**, *117*, 11302–11336.

[45] Wang, Y.; Lin, Y.; He, S. Y.; Wu, S. H.; Yang, C. P. Singlet oxygen: Properties, generation, detection, and environmental applications. *J. Hazard. Mater.* **2024**, *461*, 132538.

[46] Wang, L. L.; Lan, X.; Peng, W. Y.; Wang, Z. H. Uncertainty and misinterpretation over identification, quantification and transformation of reactive species generated in catalytic oxidation processes: A review. *J. Hazard. Mater.* **2021**, *408*, 124436.